nature communications

Article

https://doi.org/10.1038/s41467-025-56052-0

Transmembrane voltage-gated nanopores controlled by electrically tunable in-pore chemistry

Received: 8 July 2024

Accepted: 8 January 2025

Published online: 05 February 2025

Check for updates

Makusu Tsutsui[1], Wei-Lun Hsu[2], Chien Hsu[2], Denis Garoli[3], Shukun Weng[4], Hirofumi Daiguji[2] & Tomoji Kawai[1]

Gating is a fundamental process in ion channels configured to open and close in response to specific stimuli such as voltage across cell membranes thereby enabling the excitability of neurons. Here we report on voltage-gated solid-state nanopores by electrically tunable chemical reactions. We demonstrate repetitive precipitation and dissolution of metal phosphates in a pore through manipulations of cation flow by transmembrane voltage. Under negative voltages, precipitates grow to reduce ionic current by occluding the nanopore, while inverting the voltage polarity dissolves the phosphate compounds reopening the pore to ionic flux. Reversible actuation of these physicochemical processes creates a nanofluidic diode of rectification ratio exceeding 40000. The dynamic nature of the in-pore reactions also facilitates a memristor of sub-nanowatt power consumption. Leveraging chemical degrees of freedom, the present method may be useful for creating iontronic circuits of tunable characteristics toward neuromorphic systems.

Stochastic collisions of two or more substances provide opportunities for transforming their atomic components. Principles of chemistry govern these processes, facilitating the creation of diverse compounds with desirable properties, where factors such as pH, temperature, and pressure shape the energy landscape of reaction pathways at equilibrium. In contrast to the conventional diffusion-based chemical systems, meanwhile, nanoreactors have emerged as efficient platforms capable of controlling reaction kinetics within a nanoconfined space through mass flow control[1–3]. In particular, solid-state nanopore technology has proven useful for operando observations of the chemical synthesis of an individual nanoparticle in real time[4,5]. Motion control of the in-situ formed nanoprecipitates was also demonstrated with high length-to-diameter aspect ratio conical nanochannels[6,7], which allowed nanofluidic diodes via the transmembrane voltage-dependent clogging of the nanoscale conduits[6–10]. Inspired by these pioneering works, we herein report tunable chemical reactions by electrical manipulation of ion transport in a small hole for advanced fluidic devices. This method employs a 40 nm-thick dielectric membrane hosting a nanopore connecting two distinct ionic reactant solutions for precise manipulations of the ion electromigration to enable reversible precipitation/dissolution reactions of a metal compound layer (Fig. 1). The resulting dynamic opening and closure of the fluidic channel enable a spectrum of ion transport behaviors ranging from fluidic diodes[11] regulating ion flux with a high rectification ratio over 10^4 to ionic memristors[12–18] characterized by sub-nanowatt energy consumption. Alternatively, the in-pore reaction can be configured to synthesize insoluble precipitates through the choice of ion valency allowing enhanced sensor spatial resolution for resistive pulse detections of biomolecules.

Results

Strong ionic rectifications under salinity difference

Nanopores were fabricated by sculpting holes of various diameters (d_{pore}) in a 40 nm-thick SiN_x membrane on a Si wafer using electron

[1]The Institute of Scientific and Industrial Research, Osaka University, Mihogaoka 8-1Ibaraki Osaka 567-0047, Japan. [2]Department of Mechanical Engineering, The University of Tokyo, 7-3-1, HongoBunkyo-ku Tokyo 113-8656, Japan. [3]Istituto Italiano di Tecnologia, Optoelectronics Research Line, Morego 30, I-16163 Genova, Italy. [4]Dipartimento di scienze e metodi dell'ingegneria, Università degli studi di modena e reggio emilia, 42122 Reggio emilia, Italy.
e-mail: tsutsui@sanken.osaka-u.ac.jp; kawai@sanken.osaka-u.ac.jp

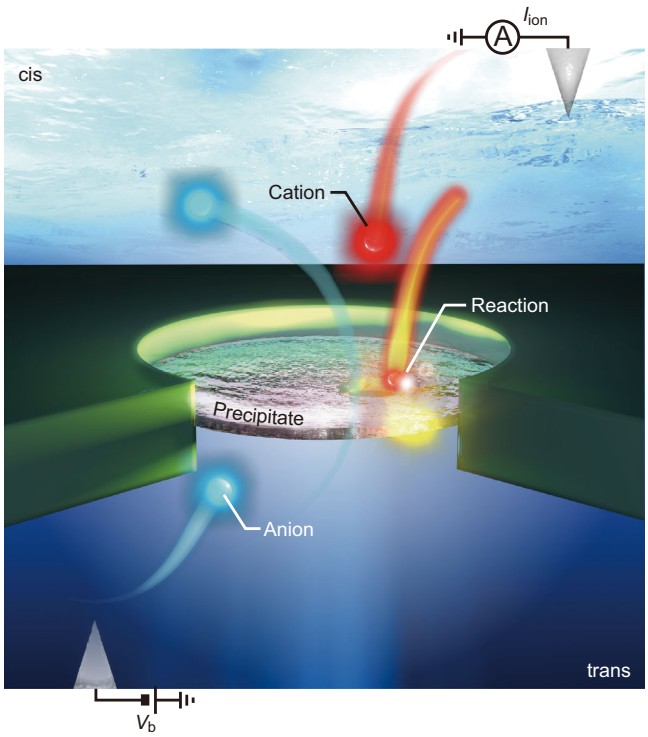

Fig. 1 | Transmembrane voltage-controlled precipitation reactions inside a nanopore. A Schematic illustration depicting ion transport-triggered precipitation reaction inside a nanopore. The transmembrane voltage V_b induces the electromigration of ions. The resulting cation flow causes chemical reactions to form or dissolve a metal phosphate compound in a voltage-controllable fashion. The associated dynamic change in the effective pore size is measured by the ionic current I_{ion}.

beam lithography and reactive ion etching[19]. Ionic current (I_{ion}) was measured under transmembrane voltage (V_b) with a scan rate (r_{scan}) of 65 mV s^{-1} in phosphate-buffered saline containing 1.37 M NaCl at pH 7.4 (hereafter, NaCl solution refers to the phosphate buffer unless otherwise denoted). The observed ohmic behavior showed a slope ($G_{pore} = I_{ion}V_b^{-1}$) of 3.2 µS (Fig. 2a), consistent with Maxwell–Hall's model[20,21] for d_{pore} of 300 nm and solution resistivity (ρ_{NaCl}) of 0.08 Ω m (with negligible contributions of surface conduction due to the relatively large pore size compared to the sub-nanometer scale Dukhin length in the high ionic strength saltwater[22]). On the other hand, replacing NaCl at the *cis* compartment with other salts resulted in asymmetry in the I_{ion}–V_b characteristics. In the case of KCl and CsCl (2 M concentration unless otherwise stated; see also Supplementary Table 1 for the solution pH measured using a pH meter (F-71S, HORIBA)), for instance, G_{pore} tended to be higher under negative voltages. $MgCl_2$ also rendered a similar feature yet with an opposite trend in the conductance at $V_b < 0$.

Here, the ionic conductivity is affected by the concentrations and mobilities of cations and anions. From this viewpoint, it is noticeable that positive transmembrane voltage generates electromigration flow of Na^+ through the pore no matter the salts in the cis, giving rise to a similar conductance at $V_b > 0$ (Fig. 2a). Likewise, the conductance at negative voltages can be explained by the distinct mobilities of the three cations, as shown by the linear relationship with G_{pore} under homogeneous salt solutions (Fig. 2b). It, thus, demonstrates V_b-controlled selective transport of cations in the nanopore under the salt difference across the membrane.

In stark contrast to the ohmic behaviors, $CaCl_2$ and $MnCl_2$ exhibited strong suppression of the ionic current at $V_b < 0$ (Fig. 2c). Strikingly, the rectification ratio $r_{rec} = |I_{+1}/I_{-1}|$ reached over 40,000, where I_{+1} and I_{-1} are I_{ion} at $V_b = 1$ V and −1 V, respectively (Fig. 2d, see also Supplementary Figs. 1–7). Increasing the number of pores in a membrane can even enhance r_{rec} further unless the porosity is made not too large as the inter-pore interactions[23,24] serve to weaken the rectification features (Supplementary Fig. 8). Although still not competitive to solid-state electronic devices, this r_{rec} is more than an order of magnitude higher than the state-of-the-art nanofluidic diodes[25,26] relying on permselective transport[27] and electroosmotic flow mechanisms[28].

The strong rectification behaviors were also revealed as dependent on the size of the nanofluidic channels as well as the voltage scan speed (Supplementary Figs. 9–12). Denoted by r_{rec} in Fig. 2d, for instance, the I_{ion} suppression at negative V_b was completely absent in 3 µm-sized pores irrespective of the salts tested under r_{scan} of 65 mV s^{-1} (Supplementary Figs. 9c and 10). Slowing down the sweep rate by order of magnitude, on the other hand, the micropores exhibited rectification characteristics for $CaCl_2$ with r_{rec} amounting to over 10,000 (Supplementary Figs. 9d and 11). Meanwhile, 100 nm nanopores reproduced the high-r_{rec} ion transport properties with $CaCl_2$ and $MnCl_2$ at 65 mV s^{-1}. Notably, $MgCl_2$ also gave rise to the ionic rectification (Supplementary Figs. 3b and 13) suggesting that smaller size of the fluidic channels with slower voltage scan rates facilitate the extreme ionic current blockade at $V_b < 0$.

The suppressed I_{ion} state was found stable at around 100 pA for over 100 s (Supplementary Fig. 14) implying nearly complete blockage of the translocation of high-concentration cations and anions under the negative voltages. It was previously found that permselective ion transport causes ionic rectification via the involved concentration polarization at the orifices[27]. However, the pores in the present study are considerably larger compared to the sub-nanometer-scale Debye screening length in the dense salt solutions of over 1 M anticipating negligible ion selectivity[28]. Analogously, ion–ion interactions cause minor effects on the ionic conductance as they generally become notable only in single-digit nanopores[29]. Electroosmotic flow also fails to explain the phenomenon as it works only under large transmembrane salinity difference[28,30]. This was also confirmed by the ionic current measurements under salinity difference of the same types of salts at the *cis* and *trans* showing only weak rectification characteristics due to the electroosmosis mechanism (Supplementary Fig. 15). Hence, it needs to be elucidated what mechanism is responsible for the strong inhibition of the ion flow.

In this regard, it is pointed out that the ionic strength of the salt solutions is over 1 M. Particular cations may thus be prohibited from passing through the pore as it raises the ion concentration of the NaCl buffer to above the solubility limit[31,32]. Nonetheless, the I_{ion} blocking was still present even when lowering the salt concentration c_{trans} at the *trans* to below 0.01 M denying the possible roles of the solubility (Supplementary Fig. 16). Furthermore, the I_{ion} suppression occurred even with only salinity difference, i.e., *cis* and *trans* filled with water containing one specific type of salt at different concentrations (Supplementary Figs. 15 and 17). These observations anticipated formations of a matter via V_b-derived reactions that occluded the space for the electromigration of ions through the pores. In fact, white substance appeared upon mixing bulk solutions in a flask (Supplementary Fig. 18), which is ascribable to precipitation reactions of divalent and trivalent cations with the phosphoric acid included in the electrolyte buffer to form metal phosphates, as also confirmed by X-ray photoelectron and Raman spectroscopy analyses (Supplementary Figs. 19 and 20)[7,33].

Roles of in-pore chemical reactions

The role of phosphoric acid was verified by replacing the phosphate-buffered saline at the *trans* with phosphate-free NaCl water of salt concentration 1.4 M. The ionic current characteristics were revealed as featureless denoting the absence of the precipitation reactions in the

https://doi.org/10.1038/s41467-025-56052-0

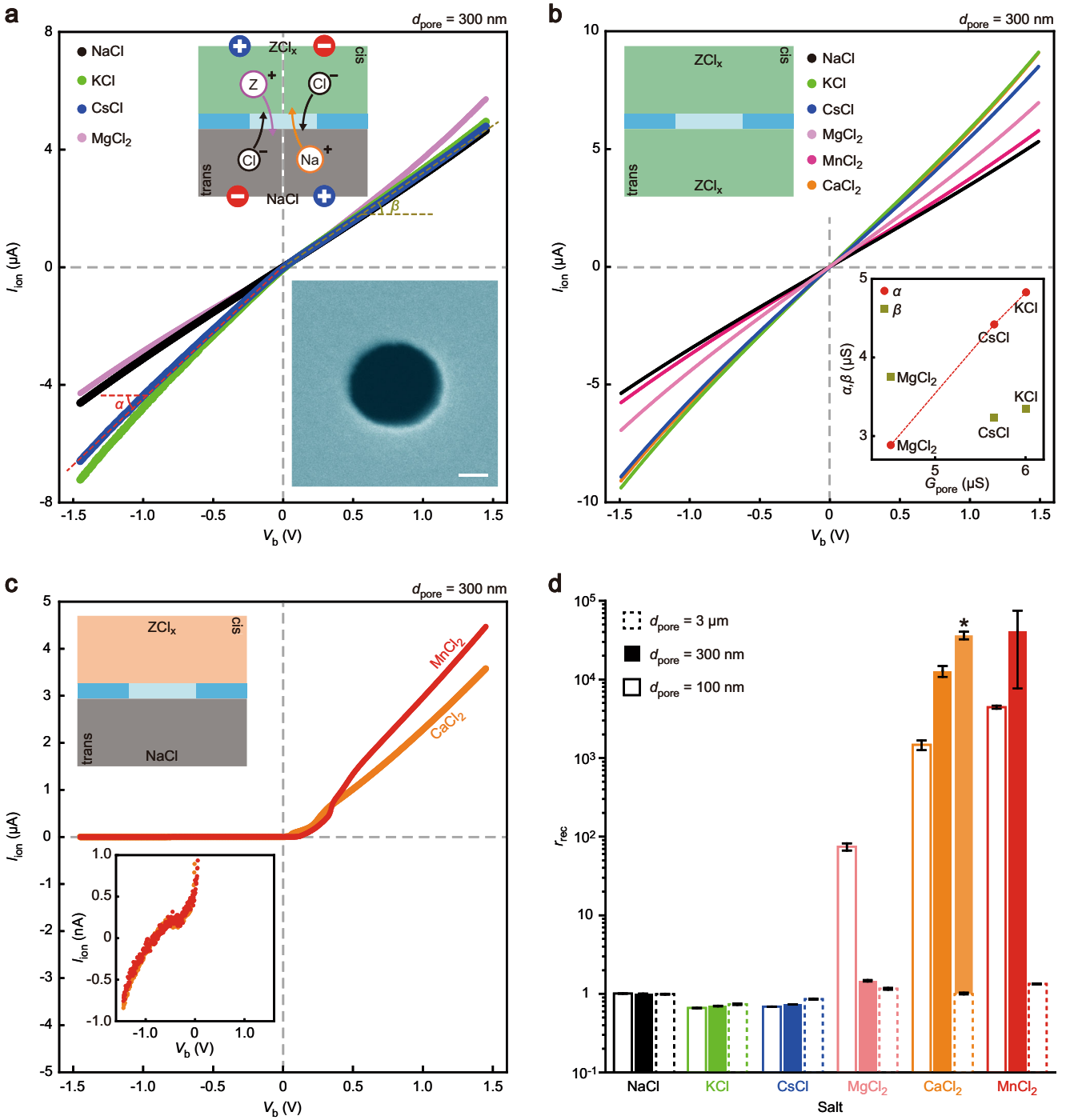

Fig. 2 | Ionic current rectifications in nanopores under salt difference. a I_{ion} versus V_b characteristics obtained for a 300 nm diameter pore with the *cis* side filled with 1.37 M NaCl (black), 2 M KCl (green), 2 M CsCl (blue), and 2 M $MgCl_2$ (pink) while the *trans* side always with 1.37 M NaCl (pH 7.4). Red and dark yellow dashed lines are linear fitting to the plots at the negative and positive V_b regimes, respectively, which give the slopes α and β. Inset sketch depicts the difference in the electromigration of cations and anions under negative (left) and positive V_b (right). The scanning electron micrograph displays a 300 nm nanopore. Scale bar denotes 100 nm. **b** The ion transport properties under no salt difference (NaCl (black), KCl (green), CsCl (blue), $MgCl_2$ (pink), $MnCl_2$ (magenta), and $CaCl_2$ (orange)). The salinity was also the same at *cis* and *trans* (1.37 M for NaCl and 2 M for the rest of the salts). The inset plots α (red) and β (dark yellow) in **a** as a function of the nanopore conductance G_{pore} with no salt difference. **c** Ionic current rectifications were observed for 2 M $CaCl_2$ (orange) and $MnCl_2$ (red) at the *cis* with the *trans* filled with 1.37 M NaCl (pH 7.4). Inset is a magnified view of the suppressed ionic current at $V_b < 0$ V. **d** The rectification ratio r_{rec} at $V_b = \pm 1$ V obtained from the ionic current characteristics measured in pores of three different diameter d_{pore} and various salts at the cis (with the trans filled with 1.37 M NaCl at pH 7.4). r_{rec} tends to be close to 1 when the I_{ion}–V_b characteristics show ohmic behaviors. On the other hand, $r_{rec} > 1$ denotes I_{ion} suppression at negative transmembrane voltage. The high r_{rec} for the 3 μm micropore with $CaCl_2$ is a result obtained at a low V_b scan rate of 6.5 mV s^{-1} (marked by an asterisk), while the other data are of 65 mV s^{-1}. Note that the rectification ratio attains over 40,000 for the case of a 300 nm-sized nanopore with a $MnCl_2$/NaCl configuration. Each error bar denotes the standard deviation of three independent I_{ion}–V_b measurements performed on a nanopore. (The results in Supplementary Figs. 3 and 6 are not included.) Source data are provided as a Source Data file.

range of pH from 5.5 to 11.7 (Supplementary Fig. 21). Consistently, no precipitates were found in the mixture solutions (Supplementary Fig. 22). These results unambiguously indicated the in-pore formations and dissolutions of metal phosphates via the reaction between the divalent cations and phosphoric acids as the cause of the extreme ionic current rectification behaviors. In the case of $CaCl_2$/phosphate buffer configuration, for instance, the electromigration of Ca^{2+} at negative voltages leads to the local synthesis and growth of the phosphate layer to almost completely seal the pore, and the reverse reaction in the acidic $CaCl_2$ solution dissolves the nanoprecipitate upon ceasing the Ca^{2+} supply at $V_b > 0$. As such, solution pH plays a role in the reaction equilibrium, where the rectifying behaviors were demonstrated to disappear under highly acidic conditions prohibiting the in-pore precipitations of the metal phosphates (Supplementary Fig. 24).

To further verify the reaction-mediated ionic conductance transition mechanism, we performed simultaneous measurements of I_{ion} and the temperature T_{pore} at a nanopore to detect the local heat dissipation involved in the chemical processes (Fig. 3a). For this, we embedded a nanowire thermocouple[34] at the proximity of a 60 nm-sized pore. We observed rectifying behavior upon scanning V_b with $CaCl_2$ solution at the *cis* (Supplementary Fig. 25a, b). At the same time, the thermovoltage V_t at the thermocouple was recorded, from which T_{pore} was deduced through the relation $T_{pore} = 5.3 \times 10^6 V_t$ obtained in the calibration measurements[35]. T_{pore} was found to increase steadily with V_b in the positive voltage regime denoting the local Joule heating by ion transport (see also Supplementary Fig. 26 for the case of CsCl)[36–38]. In contrast, the nanopore temperature showed a temporal increase to above room temperature upon decreasing V_b to below 0 V (Fig. 3a), which is not attributable to the ionic heat dissipation since I_{ion} is strongly suppressed under the negative voltage. Instead, it suggests the dissipation of heat generated in the precipitation process. Analogously, T_{pore} exhibited a decrease when scanning back V_b toward 0 V, indicative of local cooling by heat adsorption during the calcium phosphate dissolution. No such trait emerged for $MgCl_2$ despite its similar ionic current characteristics to $CaCl_2$ (Fig. 3b, c, see also Supplementary Fig. 25c, d), presumably due to the relatively small reaction enthalpy involved in anticipating negligible heat dissipation in the precipitation/dissolution stages. Although the synthesis of the metal phosphates in non-alkaline media is generally a complicated process for predicting whether the reactions inside the nanopore should be endothermic or exothermic[39,40], the overall results consistently suggest the ion transport-mediated in-pore precipitation/dissolution as a primary factor of the extreme I_{ion} rectifications.

Memory effects in chemical reaction-mediated ion transport

The time-evolving nature of the voltage-controlled precipitation/dissolution provides varying ion transport properties. For example, it induces the V_b scan rate dependence of the I_{ion} characteristics seen in the micropores (Fig. 4, see also Supplementary Fig. 27). Interestingly, once the precipitation clogging was examined under the slow V_b scan speed of 6.5 mV s^{-1}, the I_{ion} suppression became operatable at 65 mV s^{-1}, perhaps due to the residual precipitates on the wall surface that served as crystal seeds for facilitating the growth of phosphates[10,41]. Whereas this transformed the microfluidic channel to a diode, it could also be returned to a resistor by eliminating the precipitates on the channel wall through the repetitive voltage scans at a faster rate (650 mV s^{-1}), though not fully reversible in terms of r_{rec} presumably due to the non-dissolvable phosphates formed at the *trans* side of the membrane surface during the repetitive voltage scans (Fig. 4e). The in-pore reaction mechanism thus allows a memory effect on the ionic conductance.

Electrically tunable reaction-driven nanopore memristors

When it comes to 300 nm nanopores, the electrically tunable reactions bring memristive characteristics. The chemical reaction cycles were found as operatable in $MnCl_2$/NaCl buffer systems under various ranges of V_b scans down to ±0.2 V (Fig. 5a, b). On the other hand, the ionic current remained suppressed under ±0.1 V as the applied voltage was inadequate to activate the dissolution reaction. Furthermore, the time-evolving mode of nanoprecipitation yielded pinched hysteresis loops in the I_{ion}–V_b curves, which are generally considered as a fingerprint of a memristor (Fig. 5c)[42]. Indeed, the nanopore conductance at 0.1 V could be modulated by external stimuli with sub-nanowatt power, where the potentiation and depression were implemented via positive and negative V_b pulses (Fig. 5d) that induced sequential dissolution and precipitation of metal phosphates inside the nanopore for over 1000 s (Fig. 5e). Similar characteristics were also found in $CaCl_2$/NaCl buffer systems, but at a relatively high conductance regime reflecting its reaction equilibrium distinct to that in the $MnCl_2$ solution (Supplementary Fig. 28). Here we add the importance of a training process to obtain the stable memristive characteristics. More specifically, V_b scans were implemented multiple times to reproducibly form a phosphate layer inside a nanopore that served to initialize the memristor state prior to the subsequent potentiation/depression cycling (Supplementary Figs. 29, 30). Without this pretreatment, the nanopore memristors tend to be non-controllable by the voltage pulses. Such fine control of the nanopore conductance may not be achievable with the conical nanopore approach[6–10] as it requires a formidable task of precise manipulation of the Brownian motion of a precipitated nanoparticle under the influence of the electrostatic and hydrodynamic drag forces[43]. With the reaction degrees of freedom controllable by the choice of salt solution properties and membrane material designs, this approach would allow nanofluidic memristor building blocks of tunable characteristics for neuromorphic computations.

Single-molecule sensing by nanoprecipitated nanopores

Besides the iontronics applications, the in-pore precipitation can be useful for shrinking nanofluidic channels. Unlike the cases for the divalent cations where the nano-precipitates can be dissolved during positive voltage sweeps, electromigration of trivalent ions like Al^{3+} tended to form more robust phosphate layers that led to partial clogging of nanopores as seen by gradual drops in I_{ion} during repetitive V_b scans with $AlCl_3$ in the *cis* (Fig. 6a, see also Supplementary Fig. 31). As a consequence, G_{pore} of 300 nm nanopores decreased by about two orders of magnitude (Fig. 6b, c). The low conductance state remained stable upon replacing the $AlCl_3$ solution with NaCl buffers of various salt concentration c_{ion}. Scanning electron microscopy observations after the precipitation reaction revealed the aluminum phosphate formed in the nanopore (Fig. 6d inset). Whereas stable at the neutral conditions, the precipitated layer was also revealed as readily removable with acid that enabled a binary control of d_{pore} by the solution pH (Supplementary Fig. 31).

We evaluated the structure and ion transport properties of the phosphate-clogged nanopore. G_{pore} in dilute NaCl solutions was observed to level off at below 10^{-2} M signifying the dominant contributions of counterion transport on I_{ion} (Fig. 6d)[44]. Theoretical model[22] describes the ion transport characteristics as

$$G_{pore} = \left(\sigma \frac{4L_{mem}}{\pi d_{pore^2}} \times \frac{1}{1 + \frac{4L_D}{d_{pore}}} + \frac{2}{\alpha d_{pore} + \beta L_D} \right)^{-1} \quad (1)$$

where L_{mem} and L_D are the membrane thickness and the Dukhin length, respectively. Further, L_D can be approximated as $L_D = \sigma_{wall}/(2ec_{ion})$ with

https://doi.org/10.1038/s41467-025-56052-0

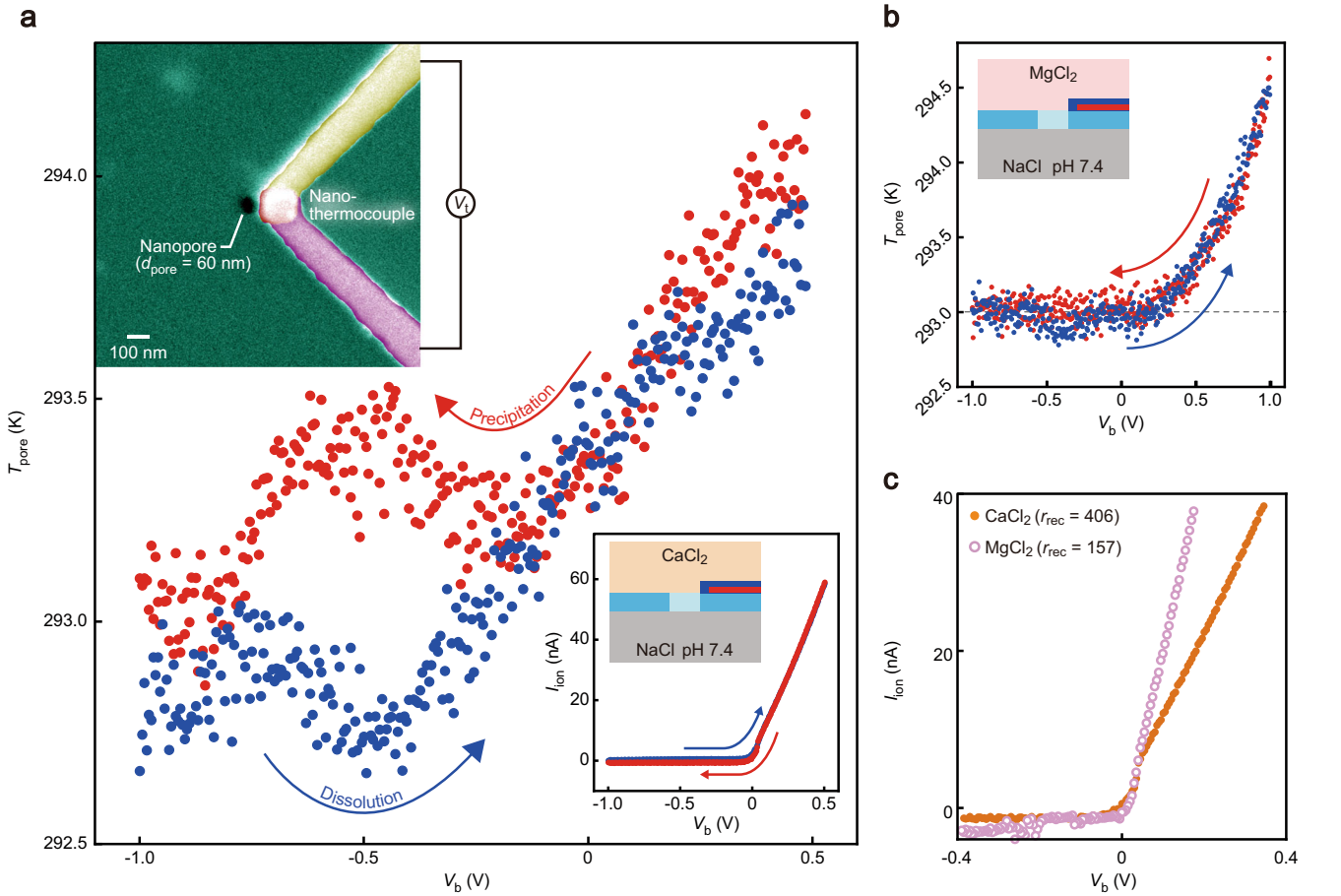

Fig. 3 | Cation flow-mediated precipitation/dissolution reactions of metal phosphates in nanopores. a Change in the nanopore temperature T_{pore} during voltage scans for a 60 nm nanopore with the $CaCl_2$/NaCl configuration. Red and blue plots were recorded during negative and positive V_b scans, respectively. Inset electron micrograph at the upper left shows the device used for the measurement, where the Au/Pt thermocouple was used to probe the temperature at the point of contact in the vicinity of the pore. The plots at the lower right are the transmembrane ionic current simultaneously recorded with the thermovoltage V_t at the thermocouple representing rectifying behavior. **b** T_{pore}–V_b characteristics acquired for a $MgCl_2$/NaCl system. Arrows denote the voltage scan directions (positive (blue) and negative (red)). No notable change in the nanopore temperature was observed reflecting the small reaction heat generated in the precipitation/dissolution of magnesium phosphates. **c** Simultaneously recorded I_{ion}–V_b characteristics demonstrating ionic current rectification similar to the case in the $MgCl_2$/NaCl system (pink open circles). The result for the $CaCl_2$/NaCl configuration is also shown (orange solid circles). Voltage scan rate is 1 mV s^{-1} in (**d**–**f**).

the surface charge density σ_{wall} at the pore wall. From this, the effective diameter and surface charge density of the phosphate-blocked nanopore are estimated to be 20 mC m^{-2} and 10 nm, respectively, where we considered the proton effect of fully dissolved carbon dioxide to alter the pH from 7.4 to 5.6 for the weak buffer capability in the diluted solutions (the comparatively larger pore size than those formed in the $MnCl_2$ and $CaCl_2$ solutions is presumably due to the difference in the reaction equilibrium under the given conditions). Since the result cannot elucidate the polarity of the pore wall, we also examined the I_{ion} measurements under salinity difference. Lowering the ion concentration at the cis (c_{cis}) than that at the trans (c_{trans}), the diffusion voltage V_{dif} (calculated by subtracting the redox potential V_{red} from V_{open}) became more negative (Supplementary Fig. 32) in accordance with the Nernst equation (Fig. 6e) giving $V_{dif} = S_{ion}(k_BT/e)\ln(c_{cis}/c_{trans})$[45,46]. Here, the selectivity factor S_{ion} varies between +1 and −1 denoting perfect cation- and anion-selective transport in the fluidic channel, respectively[22,45]. For the aluminum phosphate-precipitated nanopore, S_{ion} is obtained to be +0.84 elucidating negative charges on the surface at pH 7.4, which is in contrast to the pristine 300 nm nanopore showing negligible permselectivity (Supplementary Fig. 33). It indicates potential use of the metal phosphate nanopore for osmotic energy conversion with power density[47] $P_{osm} = I_{osm}V_{dif}/(4A_{mem})$ reaching 0.13 MW m^{-2} under an assumption of 30% porosity and no inter-pore interactions[45], where I_{osm} and A_{mem} are the ionic current by osmotic flow and the effective membrane area, respectively.

The nanoscopic size of the precipitate-filled nanopore can also be used for detecting small molecules. As an example, we detected ColE1 DNA (6646 bp) in 1.37 M NaCl at V_b of 0.2 V. Whereas the I_{ion} traces were featureless in the salt water, resistive pulses were observed when the DNA was added to the *cis* compartment representing step-like features typical for the translocation of polynucleotide chains with various folding conformations[48]. Quantitatively, the histogram displays peaks at $n \times 220$ pA with $n = 1$ and 2 corresponding to non-folded and single-folded forms of DNA, respectively. This is in agreement within 11% error with the rough estimation of the blockade current assuming DNA as a cylinder of 2 nm diameter in a 40 nm-long high-aspect-ratio nanochannel in the salt water of conductivity 12.5 S m^{-1} at 0.2 V. Meanwhile, the majority of the ionic signatures (around 60%) were of simple rectangular shapes with heights around 430 pA. In fact, ColE1 DNA has closed circular forms, whose translocation anticipates the exclusion of double the volume of a double-stranded polynucleotide chain inside the nanopore[49] (the sample includes a small amount of linear DNA in addition to the circular genomes as noted in the product sheet). Here, it is noted that the gyration radius of ColE1 DNA is estimated to be 194 nm, which is much larger than d_{pore}. Therefore, the polynucleotide chains are required to be dis-

https://doi.org/10.1038/s41467-025-56052-0

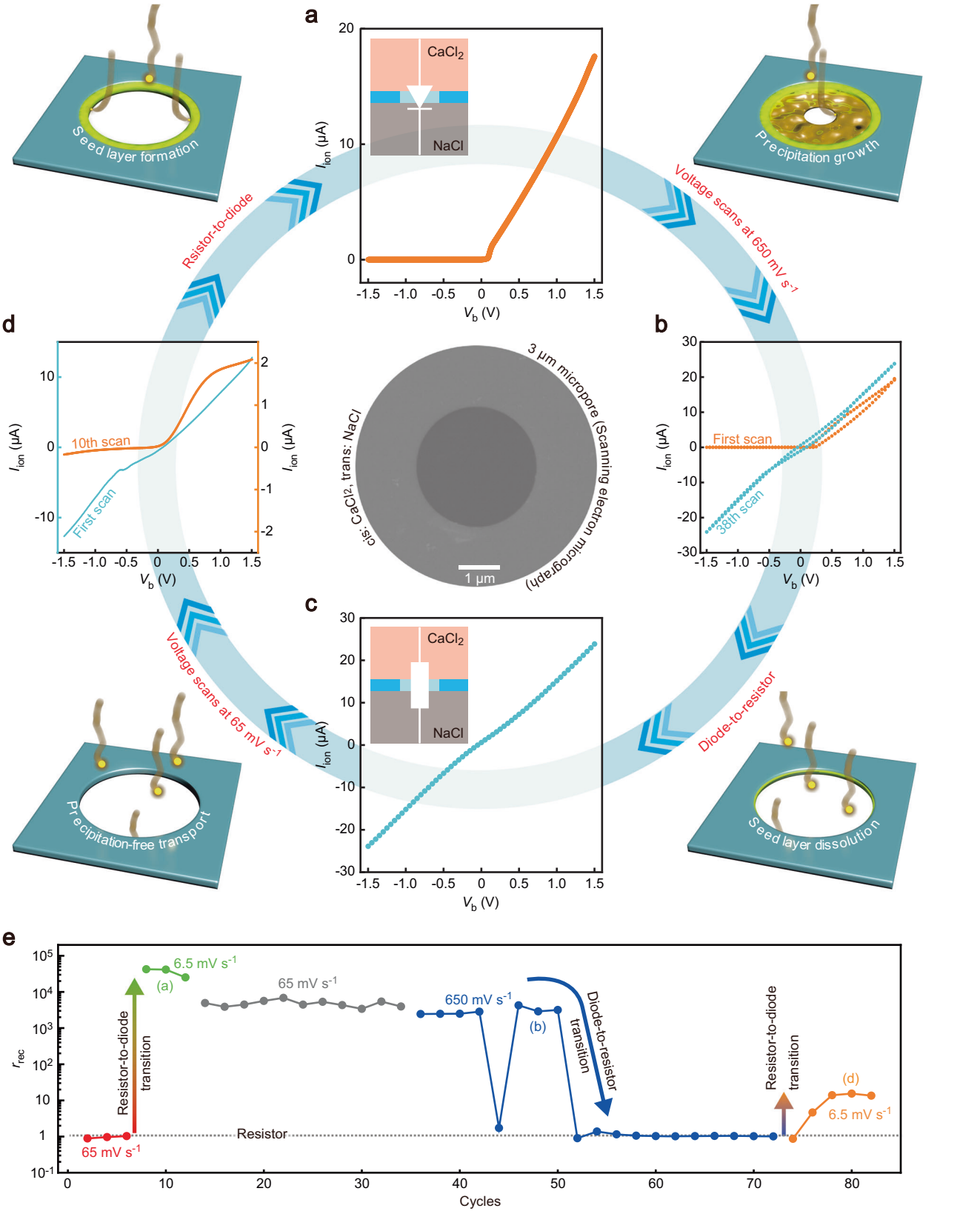

Fig. 4 | In-pore reaction-mediated memory effect in micropore ionic conductance. a Originally, a 3 μm micropore with a $CaCl_2$/NaCl arrangement behaved as an ohmic resistor at a voltage scan rate higher than 65 mV s^{-1}. However, the lower scan rate of 6.5 mV s^{-1} led to the emergence of extreme rectification suggestive of precipitation/dissolution reactions of calcium phosphates in the pore. **b** and **c** Meanwhile, repetitively scanning V_b at a faster rate (650 mV s^{-1}), the micropore gradually returned to exhibit a resistor-like behavior. **d** Subsequent scanning at 65 mV s^{-1} can further make the micropore a diode. The image at the center is a scanning electron micrograph of the micropore of 3 μm diameter. **e** Changes of the rectification behaviors upon the repetitive voltage scanning. Dotted line denotes $r_{rec} = 1$.

https://doi.org/10.1038/s41467-025-56052-0

entangled before the electrophoretic translocation[50]. In this context, the supercoiled conformations of the cyclic-formed plasmids anticipate a larger entropy barrier compared to that for the flexible linear DNA strands of the same length[51]. This would be a reason why the linear genome was detected relatively frequently in the resistive pulse measurements.

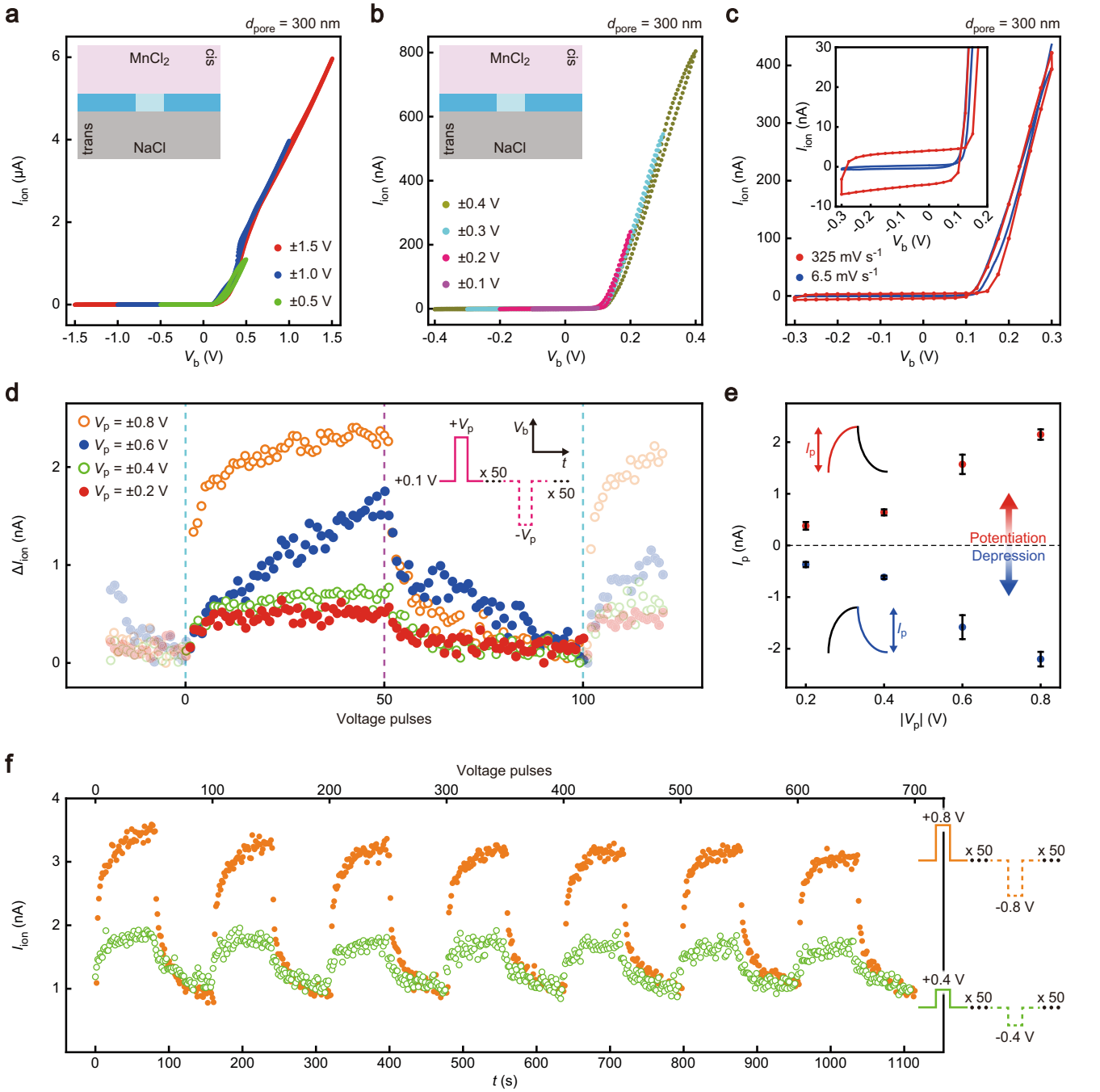

Fig. 5 | In-pore chemical reaction-driven nanofluidic memristor. a and **b** I_{ion}–V_b characteristics of a 300 nm-sized nanopore with an $MnCl_2$/NaCl configuration measured under various ranges of transmembrane voltages (±0.1 V (purple), ±0.2 V (pink), ±0.3 V (sky blue), ±0.4 V (dark yellow), ±0.5 V (green), ±1.0 V (blue), ±1.5 V (red)). The insets display the solution configuration around the nanopore membrane in skyblue, where the cis (pink) and trans (gray) compartments are filled with the $MnCl_2$ and NaCl solutions, respectively. Note the I_{ion} remains suppressed when scanning V_b between −0.1 and 0.1 V (**b**). **c** Scan rate dependence of I_{ion}–V_b displaying pinched hysteresis loops at 6.5 mV s^{-1} (blue) and 325 mV s^{-1} (red). Inset shows a magnified view of the suppressed I_{ion} states. **d** Memristive characteristics under the applications of 50 ms transmembrane voltage pulses of ±0.2 V (red), ±0.4 V (green), ±0.6 V (blue), and ±0.8 V (orange) amplitudes. ΔI_{ion} is the ionic current recorded at +0.1 V after each voltage pulsing (the baseline current was subtracted). The positive and negative pulses drive the potentiation and depression processes of the nanopore memristor via the induced in-pore dissolution/precipitation reactions. Skyblue and purple dashed lines denote the timing when the sign of the voltage pulses were switched from negative to positive and positive to negative, respectively. **e** The ionic current change I_p (defined as I_{ion} at the point when the sign of V_p was inverted) by the positive (red) and negative (blue) voltage pulses of amplitudes V_p. Error bars denote the standard deviations within four independent cycles of potentiation/depression processes on a nanopore. Source data are provided as a Source Data file. **f** Potentiation/depression of the nanopore memristors under the voltage pulses of V_p = ±0.8 V (orange solid circles) and ±0.4 V (green open circles). Read voltage was +0.1 V.

https://doi.org/10.1038/s41467-025-56052-0

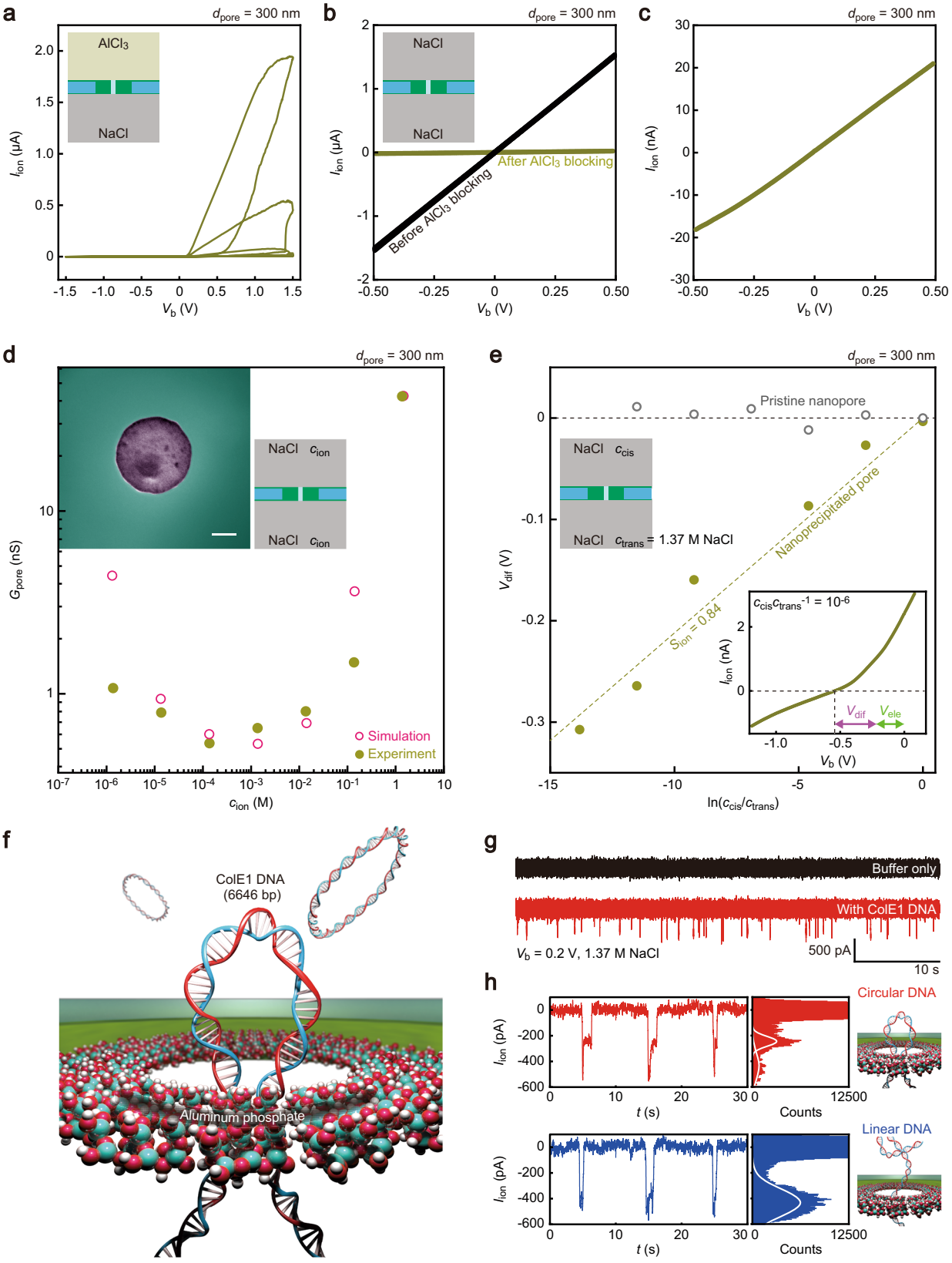

Discussion

Electromigration of ions was demonstrated as capable of inducing electrically tunable metal phosphate precipitation/dissolution in a pore for advanced nanofluidic devices including diodes and memristors. In stark contrast to conventional nanofluidic devices operating within nano- and atomic-scale systems[52–54], the present method can benefit from the easy-to-fabricate large channel size to gain improved diode performance promoting widespread feasibility without requiring any sophisticated facilities. The demonstrated control over precipitation reactions in multipores also justifies its scalability for integrated circuits composed of iontronic building blocks[55] as well as nanoporous membranes for blue energy harvesting[56].

Fig. 6 | Single-molecule sensing using a precipitated nanopore. a I_{ion}–V_b characteristics of a 300 nm-sized nanopore with an $AlCl_3$/NaCl configuration. The ionic conductance decreased steadily when repeating the voltage scans. **b** The ionic current curves in 1.37 M NaCl solution at pH 7.4 before (black) and after (dark yellow) the measurements with $AlCl_3$. **c** Magnified view of (**b**) depicting the lowered nanopore conductance after the aluminum phosphate precipitation. **d** The conductance G_{pore} of the aluminum phosphate-precipitated nanopore in NaCl solutions of various salt concentrations c_{ion} (dark yellow solid circles). Schematic illustration displays the solution configuration around the nanopore membrane, where the SiN_x membrane and the precipitated layer are shown in skyblue and green, respectively. Simulation using the theoretical model in ref. 22 under the assumed fully dissolved CO_2 is shown by pink open circles. Inset is a false-colored scanning electron micrograph taken after the precipitation reaction. Scale bar denotes 100 nm. **e** Diffusion voltage V_{dif} obtained for the nanoprecipitated nanopore under salinity difference applied by changing the NaCl concentration at the cis (c_{cis}) while keeping the trans at c_{trans} = 1.37 M. Dark yellow dashed line is a Nernst equation fit to the V_{dif}–ln(c_{cis}/c_{trans}) plots. Results of a pristine nanopore were also shown for comparison as gray open circles. Gray dashed line points at zero diffusion voltage. Inset shows the I_{ion}–V_b curve at 10^6 salinity difference displaying open circuit voltage comprised of the redox potential V_{red} and V_{dif}. **f** Single-molecule detections of polynucleotides by ionic current. The sketch describes the electrophoretic translocation of ColE1 DNA. **g** The ionic current traces without (black) and with DNA (red) added in 1.37 M NaCl solution. Resistive pulses denote the translocation of DNA through the nanopore. **h** Resistive pulse signal waveforms. When linear DNA was detected, the ionic signals tended to exhibit stepwise changes attributed to their folding conformations (red). Two peaks were found, accordingly, in the ionic current histogram. White curves are Gaussian fittings denoting ionic current blockade by non-folded and single-folded linear DNA in the nanopore, respectively. Meanwhile, single pulses of larger amplitudes were also found, which denote the translocation of DNA in circular cyclic forms.

From a viewpoint of resistive pulse sensing, it has long been a dream for solid-state nanopore technologies to enable the formation of well-defined pore structures. Structures of biological nanopores are demonstrated as tailorable at a molecular level via the engineering of point mutations in transmembrane proteins[57]. As for the solid-state nanopores, on the other hand, electron beam milling has been demonstrated as capable of controlling the size and shape of a hole with single-nanometer resolution in a dielectric membrane. However, the fabrication can be carried out only in high vacuum[58], thus making it difficult to ensure the structure remains the same during the ionic current measurements. There is also a dielectric breakdown approach[59] that can form single-digit nanopores in situ by a simple voltage control. Nevertheless, the controllability of the number and size of pores is still considered a critical issue[60]. In contrast, the present method can seal a relatively large pore nearly completely with a leakage current of around 100 pA at 0.5 V. Leveraging the ability to open a nanopore and finely control its size by the voltage pulsing in real-time, therefore, it has a potential to become a useful tool for adjusting the pore size to fit the analytes of concern right before the resistive pulse measurements.

In addition, this approach can be readily extended to various reactions, including electrically neutral reactants by leveraging electroosmotic flow for the mass transport control[61,62]. Local electric[63], optical[64], and heat probes[65] can also be integrated to manipulate the non-equilibrium reaction processes in the reactor. With the chemical degrees of freedom, one can not only design the reactions for exploring the vast range of applications of micro- and nanofluidic systems but also seek a route toward the synthesis of unprecedented compounds.

Methods

Fabrications of SiN_x nanopores

A 4-inch silicon wafer was coated with 50 nm-thick SiN_x layers at both sides of the surface by low-pressure chemical vapor deposition. The wafer was diced into 25 mm square chips using dicer (DISCO). On the silicon chips, microelectrodes were patterned by photolithography using photoresist AZ5206 (AZ Electronic Materials). After development, a 50 nm-thick Au layer was deposited with a 5 nm-thick Cr adhesion layer by radio-frequency magnetron sputtering (Samco). The chip was then immersed in *N,N*-dimethylformamide (DMF, Wako; purity >99.5%) overnight followed by ultrasonication for lift-off. On the microelectrode side of the surface, the electron beam resists ZEP520A (Zeon) and was spin-coated and prebaked at 180 °C on a hot plate. In the resist layer, a circle of diameter d_{pore} was delineated by electron beam lithography (Elionix). After development, the resist layer was used as a mask for reactive ion etching (Samco) using HCF_3 etchant gas to drill a hole of diameter d_{pore} in the SiN_x layer. Subsequently, the chip was immersed in DMF overnight to remove the residual resist layer. The back side of the chip was spin-coated with photoresist TSMR. A 1 mm square region at the center was removed by photolithography using the microelectrode pattern at the front side as a marker. Another reactive ion etching process was carried out to partially remove the backside SiN_x layer. Aqueous solution (25 vol%) of KOH (Wako; purity > 85%) was then applied on the back-side surface and heated at 90 °C to dissolve the exposed Si layer by anisotropic etching. As a result, a 40 nm-thick SiN_x membrane with a pore of diameter d_{pore} was created.

Thermocouple-embedded nanopore fabrications

The 25 mm square silicon chips with the microelectrodes patterned on the front surface were used as substrates. A Au nanowire was formed with a 5 nm-thick Ti adhesion layer by the electron beam lithography and sputtering processes utilizing a part of the electrode pattern as a marker. Using the same marker, a Pt nanowire was subsequently patterned to form a point contact with the Au nanowire. Another electron beam lithography process was performed to delineate a nanopore of diameter 60 nm at a side of the point contact. After development, a 60 nm hole was sculpted by the reactive ion etching. The entire surface was then coated by a 20 nm-thick Cr layer by the sputtering, which served to protect the thermocouple during the post processes to penetrate the nanopore. For that, the back side of the SiN_x layer was partially removed by the photolithography and reactive ion etching. The exposed Si layer was immersed in a KOH solution and heated at 90 °C for the wet etching to form a SiN_x membrane (the Cr layer blocked the KOH solution from flowing through the nanopore to avoid any damage on the thermocouple at the front side). The chip was immersed in a Cr etchant solution to dissolve the Cr layer. Finally, the front surface was covered with a 10 nm-thick SiO_2 layer by chemical vapor deposition (Samco).

Integration of flow cells

I-shaped patterns were created in a photo-resist SU-8 3000 on a Si wafer by photolithography. On this SU-8 mold, polydimethylsiloxane (PDMS, Sylgard 184, Dow) was cured at 90 °C. A 15 mm block of the PDMS with an I-shaped trench at one side of the surface was cut out using a surgical knife. Three holes of diameter 1 mm were punched in the block that served as a place to insert an electrode for the ionic current measurements and an inlet/outlet for flowing electrolyte solutions into the pore. The PDMS block with holes was exposed to oxygen plasma along with a nanopore chip for surface activation. After that, they are put together for eternal bonding. Using the same procedure, another PDMS block was bonded to the other side of the chip.

Ionic current measurements in various salt solutions

Two Ag/AgCl rods were inserted in one of the three holes in each PDMS flow cell. The electrolyte solution was flown through the other two

holes using a pipette. The Ag/AgCl electrodes were connected to an ammeter-source unit (Keithley 6487, Keysight). Voltage ramps were biased to one of the Ag/AgCl and the transmembrane ionic current was recorded through the other Ag/AgCl via a GPIB control under a program coded in Visual Basic. Each measurement was carried out more than three times of V_b scans to obtain the arithmetic average of the ionic current, which was used for the evaluation of the in-pore reaction-mediated ionic current characteristics. When performing the measurements for various salt solutions, the Ag/AgCl electrodes were taken out from the flow cells each time before replacing the liquid and first washed with diluted phosphate-buffered saline followed by the salt solutions that were going to be measured. NaCl (purity > 99.5%), CsCl (purity > 99.0%), KCl (purity > 99.5%), $CaCl_2$ (purity > 95.0%), $MnCl_2$ (purity > 99.0%), $MgCl_2$ (purity > 98.0%), and $AlCl_3$ (purity > 98.0%) were purchased from Wako and used as received. Similarly, the dilute buffer was first flown through the inlet/outlet holes several times in the flow cells and subsequently replaced with the salt solutions of concern. These processes allowed us to avoid precipitations of phosphates in the solutions. Otherwise, the direct mixing of certain salt-water led to precipitation reaction-derived contamination of the entire fluidic channel as well as the membrane surface, including the pore wall.

Ion selectivity evaluations

Ionic current versus transmembrane voltage characteristics were measured under various salinity differences for a 10 μm micropore. The redox potential V_{red} was directly obtained from the open-circuit voltage for the negligible permselectivity of the huge pore, giving neglectable diffusion voltage. The diffusion voltage and the osmotic current were calculated from the V_{red}-subtracted I_{ion}–V_b curves of the smaller pores.

Nanopore temperature measurements

A thermocouple-embedded nanopore chip with flow cells was mounted on a sample holder. Metal pins were contacted to the two microelectrode pads connected to the Au/Pt nanowires. The pins were then wired to a nanovoltmeter (Keithley 2182A, Keysight) for recording the thermovoltage. After arranging salt solutions and Ag/AgCl electrodes by the aforementioned procedure, simultaneous measurements of the ionic current and thermovoltage were carried out by the GPIB control with visual Basic program codes. It is noted that the voltage scan rates were slow ($\approx 1\,mV\,s^{-1}$) due to the relatively long integration time required for the reliable thermovoltage measurement.

Thermocouple calibrations

The thermocouple was calibrated using the procedure described in ref. 38. The nanowire point contact was heated to pre-set temperature using an external resistive heater/thermocouple unit under PID control. After the temperature got stable, the thermovoltage at the nanowire thermocouple was recorded. The obtained thermovoltage–temperature dependence was used as a calibration curve to convert V_t to T_{pore}.

Reporting summary

Further information on research design is available in the Nature Portfolio Reporting Summary linked to this article.

Data availability

The data that support the findings of this study are available from the corresponding author upon request. Source data are provided in this paper.

References

1. Wu, C., Xing, Z., Yang, S., Li, Z. & Zhou, W. Nanoreactors for photocatalysis. *Coord. Chem. Rev.* **477**, 214939 (2023).
2. Wang, X. et al. A closed-loop catalytic nanoreactor system on a transistor. *Sci. Adv.* **9**, adj0839 (2023).
3. Swisher, J. H., Jibril, L., Petrosko, S. H. & Mirkin, C. A. Nanoreactors for particle synthesis. *Nat. Rev. Mater.* **7**, 428–448 (2022).
4. Venta, K., Wanunu, M. & Drndic, M. Electrically controlled nanoparticle synthesis inside nanopores. *Nano Lett.* **13**, 423–429 (2013).
5. Wood, M. & Zhang, B. Bipolar electrochemical method for dynamic in situ control of single metal nanowire growth. *ACS Nano* **9**, 2454–2464 (2015).
6. Siwy, Z. S., Powell, M. R., Kalman, E., Astrumian, R. D. & Eisenberg, R. S. Negative incremental resistance induced by calcium in asymmetric nanopores. *Nano Lett.* **6**, 473–477 (2006).
7. Powell, M. R. et al. Nanoprecipitation-assisted ion current oscillations. *Nat. Nanotechnol.* **3**, 51–57 (2008).
8. Yusko, E. C., Billeh, Y. N. & Mayer, M. Current oscillations generated by precipitate formation in the mixing zone between two solutions inside a nanopore. *J. Phys.: Condens. Mater.* **22**, 454127 (2010).
9. Vilozny, B., Actis, P., Seger, R. A. & Pourmand, N. Dynamic control of nanoprecipitation in a nanopipette. *ACS Nano* **5**, 3191–3197 (2011).
10. Maddar, F. M., Perry, D. & Unwin, P. R. Confined crystallization of organic materials in nanopipettes: tracking the early stages of crystal growth and making seeds for unusual polymorphs. *Cryst. Growth Des.* **17**, 6565–6571 (2017).
11. Cheng, L.-J. & Guo, L. J. Nanofluidic diodes. *Chem. Soc. Rev.* **39**, 923–938 (2010).
12. Li, J. et al. Sparse matrix multiplication in a record-low power self-rectifying memristor array for scientific computing. *Sci. Adv.* **9**, adf7474 (2023).
13. Chen, S., Zhang, T., Tappertzhofen, S., Yang, Y. & Valov, I. Electrochemical-memristor-based artificial neurons and synapses —fundamentals, applications, and challenges. *Adv. Mater.* **35**, 2301924 (2023).
14. Xiiong, T., Li, W. & Mao, L. Fluidic memristor: bringing chemistry to neuromorphic devices. *Innovation* **4**, 100435 (2023).
15. Robin, P. et al. Long-term memory and synapse-like dynamics in two-dimensional nanofluidic channels. *Science* **379**, 161–167 (2023).
16. Paulo, G. et al. Hydrophocbically gated memristive nanopores for neuromorphic applications. *Nat. Commun.* **14**, 8390 (2023).
17. Kamsma, T. M. et al. Brain-inspired computing with fluidic iontronic nanochannels. *Proc. Natl Acad. Sci. USA* **121**, e2320242121 (2024).
18. Emmerich, T. et al. Nanofluidic logic with mechano-ionic memristive switches. *Nat. Electron.* **7**, 271–278 (2024).
19. Verschueren, D. V., Yang, W. & Dekker, C. Lithography-based fabrication of nanopore arrays in freestanding SiN and graphene membranes. *Nanotechnology* **29**, 145302 (2018).
20. Garaj, S. et al. Graphene as a subnanometre trans-electrode membrane. *Nature* **467**, 190–193 (2010).
21. Wen, C. & Zhang, S.-L. On current blockade upon analyte translocation in nanopores. *J. Appl. Phys.* **129**, 064702 (2021).
22. Lee, C. et al. Large apparent electric size of solid-state nanopores due to spatially extended surface conduction. *Nano Lett.* **12**, 4037–4044 (2012).
23. Yang, J., Tu, B., Fang, M., Li, L. & Tang, Z. Nanoscale pore-pore coupling effect on ion transport through ordered porous monolayers. *ACS Nano* **16**, 13294–13300 (2022).
24. Gao, J. et al. Understanding the gian t gap between single-pore- and membrane-based nanofluidic osmotic power generators. *Small* **15**, 1804279 (2019).
25. Liu, Q. et al. A high rectification ratio nanofluidic diode induced by an "ion pool. *RSC Adv.* **10**, 7377–7383 (2020).
26. Nandigana, V. V. R., Jo, K., Timperman, A. & Aluru, N. R. Asymmetric-fluidic-reservoirs induce rectification nanofluidic diode. *Sci. Rep.* **8**, 13941 (2018).

27. Daiguji, H., Oka, Y. & Shirono, K. Nanofluidic diode and bipolar transistor. *Nano Lett.* **5**, 2274–2280 (2005).
28. Yusko, E. C., An, R. & Mayer, M. Electroosmotic flow can generate ion current rectification in nano- and micropores. *ACS Nano* **4**, 477–487 (2010).
29. Ma, J. et al. Drastically reduced ion mobility in a nanopore due to enhanced pairing and collisions between dehydrated ion. *J. Am. Chem. Soc.* **141**, 4264–4272 (2019).
30. Grau, J. J. P. et al. Fluoride-induced negative differential resistance in nanopores: experimental and theoretical characterization. *ACS Appl. Mater. Interf.* **13**, 54447–54455 (2021).
31. Luo, L., Holden, D. A., Lan, W.-J. & White, H. S. Tunable negative differential electrolyte resistance in a conical nanopore in glass. *ACS Nano* **6**, 6507–6514 (2012).
32. Laucirica, G. et al. Insight into the transport of ions from salts of moderated solubility through nanochannels: negative incremental resistance assisted by geometry. *Nanoscale* **16**, 12599–12610 (2024).
33. Ni, M. & Ratner, B. D. Nacre surface transformation to hydroxyapatite in a phosphate buffer solution. *Biomaterials* **24**, 4323–4331 (2003).
34. Tsutsui, M. et al. Peltier cooling for thermal management in nanofluidic devices. *Device* **2**, 100188 (2024).
35. Shi, L. & Majumdar, A. Recent developments in micro and nanoscale thermometry. *Microscale Thermophys. Eng.* **5**, 251–265 (2001).
36. Nagashima, G., Levine, E. V., Hoogerheide, D. P., Burns, M. M. & Golovchenko, J. A. Superheating and homogeneous single bubble nucleation in a solid-state nanopore. *Phys. Rev. Lett.* **113**, 024506 (2014).
37. Paul, S. et al. Single-bubble dynamics in nanopores: transition between homogeneous and heterogeneous nucleation. *Phys. Rev. Res.* **2**, 043400 (2020).
38. Tsutsui, M., Arima, A., Yokota, K., Baba, Y. & Kawai, T. Ionic heat dissipation in solid-state pores. *Sci. Adv.* **8**, abl7002 (2022).
39. Wang, L. & Nancollas, G. H. Calcium orthophosphates: crystallization and dissolution. *Chem. Rev.* **108**, 4628–4669 (2008).
40. Puzio, B., Menecki, M. & Kwasniak-Kominek, M. Transition from endothermic to exothermic dissolution of hydroxyapatite $Ca_5(PO_4)_3OH$-Johnbaumite $Ca_5(AsO_4)_3OH$ solid solution series at temperatures ranging from 5 to 65 °C. *Minerals* **8**, 281 (2018).
41. Peinetti, A. S., Cortez, M. L., Toimil-Molares, M. E. & Azzaroni, O. Nanoprecipitation-enhanced sensitivity in enzymatic nanofluidic biosensors. *Anal. Chem.* **96**, 5282–5288 (2024).
42. Chua, L. If it's pinched it's a memristor. *Semicond. Sci. Technol.* **29**, 104001 (2014).
43. Tsutsui, M. et al. Field effect control of translocation dynamics in surround-gate nanopores. *Commun. Mater.* **2**, 29 (2021).
44. Stein, D., Kruithof, M. C. & Dekker, C. Surface-charge-governed ion transport in nanofluidic channels. *Phys. Rev. Lett.* **93**, 035901 (2004).
45. Feng, J. et al. Single-layer MoS_2 nanopores as nanopower generators. *Nature* **536**, 197–200 (2016).
46. Zhang, S. et al. Addressing challenges in ion-selectivity characterization in nanopores. *J. Am. Chem. Soc.* **146**, 11036–11042 (2024).
47. Kim, D.-K., Duan, C., Chen, Y.-F. & Majumdar, A. Power generation from concentration gradient by reverse electrodialysis in ion-selective nanochannels. *Microfluid Nanofluid* **9**, 1215–1224 (2010).
48. Steinbock, L. J., Otto, O., Chimerel, C., Gornall, J. & Keiser, U. Detecting DNA folding with nanocapillaries. *Nano Lett.* **10**, 2493–2497 (2010).
49. Chau, C. C., Radford, S. E., Hewitt, E. W. & Actis, P. Macromolecular crowding enhances the detection of NA and proteins by a solid-state nanopore. *Nano Lett.* **20**, 5553–5561 (2020).
50. Bell, N. A. W., Muthukumar, M. & Keyser, U. F. Translocation frequency of double-stranded DNA through a solid-state nanopore. *Phys. Rev. E* **93**, 022401 (2016).
51. Harrell, C. C. et al. Resistive-pulse DNA detection with a conical nanopore sensor. *Langmuir* **22**, 10837–10843 (2006).
52. Robin, P. & Bocquet, L. Nanofluidics at the crossroads. *J. Chem. Phys.* **158**, 160901 (2023).
53. Xue, L. et al. Solid-state nanopore sensors. *Nat. Rev. Mater.* **5**, 931–951 (2020).
54. Bhardwaj, A. et al. Fabrication of angstrom-scale two-dimensional channels for mass transport. *Nat. Protoc.* **19**, 240–280 (2024).
55. Ramirez, P., Gomez, V., Cervera, J., Mafe, S. & Bisquert, J. Synaptical tunability of multipore nanofluidic memristors. *J. Phys. Chem. Lett.* **14**, 10930–10934 (2023).
56. Chu, C.-W., Fauziah, A. R. & Yeh, L.-H. Optimizing membranes for osmotic power generation. *Angew. Chem. Int. Ed.* **62**, e202303582 (2023).
57. Niu, H. et al. Direct mapping of tyrosine sulfation states in native peptides by nanopore. *Nat. Chem. Biol.* https://doi.org/10.1038/s41589-024-01734-x (2024).
58. Storm, A. J., Chen, J. H., Ling, X. S., Zandbergen, H. W. & Dekker, C. Fabrication of solid-state nanopores with single-nanometre precision. *Nat. Mater.* **2**, 537–540 (2003).
59. Waugh, M. et al. Solid-state nanopore fabrication by automated controlled breakdown. *Nat. Protoc.* **15**, 122–143 (2020).
60. Wang, Y. et al. Fabrication of multiple nanopores in a SiN_x membrane via controlled breakdown. *Sci. Rep.* **8**, 1234 (2018).
61. Baldelli, M. et al. Controlling electroosmosis in nanopores without altering the nanopore sensing region. *Adv. Mater.* **36**, 2401761 (2024).
62. Mehrafrooz, B. et al. Electro-osmotic flow generation via a sticky ion action. *ACS Nano* **18**, 17521–17533 (2024).
63. Nam, S.-W., Rooks, M. J., Kim, K.-B. & Rossnagel, S. M. Ionic field effect transistors with sub-10 nm multiple nanopores. *Nano Lett.* **9**, 2044–2048 (2009).
64. Koya, A. N. et al. Nanoporous metals: from plasmonic properties to applications in enhanced spectroscopy and photocatalysis. *ACS Nano* **15**, 6038–6060 (2021).
65. Thamdrup, L. H., Larsen, N. B. & Kristensen, A. Light-induced local heating for thermophoretic manipulation of DNA in polymer micro- and nanochannels. *Nano Lett.* **10**, 826–832 (2010).

Acknowledgements

A part of this work was supported by the Japan Society for the Promotion of Science (JSPS) KAKENHI Grant Numbers 22H01926, 22H01410, and 24K21715. M. Tsutsui acknowledges support from Kansai Research Foundation for Technology Promotion.

Author contributions

M.T., H.D., and T.K. conceived and designed experiments. M.T., W.L.H., C.H., D.G., and S.W. performed experimental studies. M.T., W.L.H., C.H., D.G., and S.W. analyzed data. M.T. and T.K. co-wrote the manuscript. All the authors discussed the data and reviewed the manuscript.

Competing interests

The authors declare no competing interests.

Additional information

Supplementary information The online version contains supplementary material available at https://doi.org/10.1038/s41467-025-56052-0.

Correspondence and requests for materials should be addressed to Makusu Tsutsui or Tomoji Kawai.

Peer review information *Nature Communications* thanks Stefan Tappertzhofen and the other, anonymous, reviewer(s) for their contribution to the peer review of this work. A peer review file is available.